



Co-rotating Taylor–Couette flow enclosed by stationary disks

M. Heise^{1,†}, Ch. Hoffmann², Ch. Will¹, S. Altmeyer², J. Abshagen¹
and G. Pfister¹

¹Institut für Experimentelle und Angewandte Physik, Universität Kiel, D-24098 Kiel, Germany

²Institut für Theoretische Physik, Universität des Saarlandes, D-66123 Saarbrücken, Germany

(Received 15 April 2012; revised 23 July 2012; accepted 23 October 2012)

We report results of a combined numerical and experimental study on axisymmetric and non-axisymmetric flow states in a finite-length, co-rotating Taylor–Couette system in the Taylor vortex regime but also in the Rayleigh stable regime for moderate Reynolds numbers (≤ 1000). We found the dominant boundary-driven axisymmetric circulation to play a crucial role in the mode selection and the bifurcation behaviour in this flow. A sequence of partially hysteretic transitions to other axisymmetric multi-cell flow states is observed. Furthermore, we observed spiral states bifurcating via a supercritical Hopf bifurcation out of these multi-cell states which strongly determine the shape of the spiral. Finally, an excellent agreement between experimental and numerical results of the full Navier–Stokes equations is found.

Key words: bifurcation, nonlinear dynamical systems, vortex flows

1. Introduction

Hydrodynamic instabilities have been preferentially studied with idealized boundary conditions, such as the centrifugal instability in Taylor–Couette flow. It is characterized by a flow of a viscous fluid in the gap between two rotating cylinders (Tagg 1994), where, under the assumption of infinite axial length, Taylor vortices appear from a pitchfork bifurcation with a well-defined critical wavelength (Taylor 1923). Benjamin and Mullin discovered that the pitchfork bifurcation is destroyed in a physical flow owing to the presence of stationary endwalls, and the relevance of these axial ends for bifurcation events in Taylor–Couette flow has been revealed in a series of subsequent studies (Benjamin 1978*a,b*; Benjamin & Mullin 1981; Mullin 1982; Tavener & Cliffe 1991; Cliffe, Kobine & Mullin 1992).

Physically, the no-slip condition at the stationary endwalls reduces the azimuthal velocity near these walls compared to the flow in the bulk, generating a boundary

[†] Email address for correspondence: heise@physik.uni-kiel.de

layer at bottom and top, which is directed radially inwards and recirculates in the bulk of the system (Czarny *et al.* 2003). While the so-called Ekman vortices have almost the size of Taylor vortices for a stationary outer cylinder, recent studies on independently rotating cylinders have revealed that a large-scale circulation consisting of two cells can emerge at the boundary layer near the ends (Hollerbach & Fournier 2004). Moreover, multiple localized axisymmetric states can appear from such a large-scale boundary-driven Ekman flow (Abshagen *et al.* 2010) and this cellular flow can undergo time-dependent instabilities towards non-axisymmetric spiral vortices. Localized spirals have been observed near the endwalls in a counter-rotating flow (Andereck, Liu & Swinney 1986; Heise *et al.* 2008a) while global spirals are found numerically in the large-scale circulation of solid-body rotation over stationary endwalls (Avila *et al.* 2008).

In this article, we elucidate the influence of the boundary-driven circulation on co-rotating Taylor–Couette flow. The flow between co-rotating cylinders has been studied mainly with a focus on nonlinear pattern formation (Nagata 1988; Cross & Hohenberg 1993; Hegseth, Baxter & Andereck 1996), with an emphasis on magnetohydrodynamical phenomena with respect to astrophysical application (Hollerbach & Rüdiger 2005; Duschl & Britsch 2006; Ji *et al.* 2006; Stefani *et al.* 2006) and in turbulent flows (Paoletti & Lathrop 2011; van Gils *et al.* 2011). The boundary-driven circulation studied here is generated by stationary endwalls at bottom and top. Recent attempts have been made to quantitatively reduce the boundary-driven circulation by rotating endwalls in the context of bifurcation studies (Abshagen *et al.* 2004; Heise *et al.* 2009) as well as in astrophysical application (Burin *et al.* 2006; Schartman, Ji & Burin 2009). However, the endwalls remain an integral part of the physical realization of Taylor–Couette flow that qualitatively differs in bifurcation behaviour from circular Couette flow (Benjamin 1978a,b; Benjamin & Mullin 1981; Heise *et al.* 2009; Abshagen *et al.* 2010). Here, we focus on the underlying axisymmetric flow of finite co-rotating Taylor–Couette flow as well as the dynamics and the bifurcation behaviour of spiral modes that appear above and even in the Rayleigh stable regime for inviscid flows. In this co-rotating flow regime the axially infinite, circular Couette flow (CCF) becomes centrifugally unstable and axisymmetric toroidally closed cells (Taylor vortices) appear. Their onset is well-approximated by the Rayleigh criterion, given by $R_1 = 2R_2$ for our radius ratio (R_1 and R_2 are defined below).

Therefore, precise Taylor–Couette experiments and numerical simulations of the full Navier–Stokes equations are performed and compared in the Rayleigh stable and Rayleigh unstable regime. We focus on the influence of the boundary-driven circulation on co-rotating Taylor–Couette flow.

2. The system

In the Taylor–Couette system, a Newtonian fluid of kinematic viscosity ν fills the annular gap between two concentric, independently rotating cylinders (inner, outer radii $r_{1,2}$; angular velocities $\Omega_{1,2}$, system length L , gap width $d = r_2 - r_1$). Non-rotating rigid lids close the gap and serve as axial endwalls. Geometric parameters are the aspect ratio $\Gamma = L/d$ and the radius ratio which is fixed throughout this article at $\eta = r_1/r_2 = 0.5$.

2.1. Numerical simulations

The system is governed by the Navier–Stokes equations (NSE). Cylindrical coordinates r, φ, z are used to decompose the velocity field into a radial component u , an

azimuthal one v , and an axial one w . All variables and parameters are dimensionless (lengths are scaled by the gap width d , times t by the radial diffusion time d^2/ν , and the pressure p by $\rho\nu^2/d^2$) leading to the dimensionless NSE

$$\partial_t \mathbf{u} = \nabla^2 \mathbf{u} - (\mathbf{u} \cdot \nabla) \mathbf{u} - \nabla p. \quad (2.1)$$

The radial (no-slip) boundary conditions for v are given by the Reynolds numbers $R_1 = r_1 \Omega_1 d/\nu$ and $R_2 = r_2 \Omega_2 d/\nu$, which are just the reduced azimuthal velocities of the respective cylinder surface.

The numerical simulations were done with the G1D3 code (Altmeyer *et al.* 2010), a combination of a finite-differences method in t , r , and z and a Galerkin expansion in φ . Since we studied finite-length cylinders with lids bounding the annulus axially, we do not use here a spectral decomposition in the axial direction. The discretization (a forward time, centred space (FTCS) algorithm) has been done on staggered grids in the r – z plane following the procedure of Hirt, Nichols & Romero (1975). It yields simple expressions for the derivatives, it does not require boundary conditions for the pressure, and it avoids difficulties with boundary conditions for more than one velocity field component at the same position. We used homogeneous grids with discretization lengths $\Delta r = \Delta z = 0.05$ which have been shown to be more accurate than non-homogeneous grids. Time steps were $\Delta t < 1/3600$.

Azimuthally, all fields $f = u, v, w, p$ were expanded as

$$f(r, \varphi, z, t) = \sum_{m=-m_{\max}}^{m_{\max}} f_m(r, z, t) e^{im\varphi}. \quad (2.2)$$

For the flows investigated here, a truncation of the above Fourier expansion at $m_{\max} = 8$ has been verified to properly resolve the anharmonicities in the fields. Deeper investigations have shown that the (cylindrical) system always prefers structures with smaller azimuthal wavenumbers m . This also holds for the subcritical case where $m \neq 0$ modes (originating from fluctuations) are excited by $m = 0$ modes (originating from the endwalls) through nonlinearities (cf. Altmeyer *et al.* 2010 for the interaction of $m = 0$ and $m \neq 0$ structures). The azimuthal Fourier spectrum effectively vanishes for $m > 2$.

The system of coupled equations for the amplitudes $f_m(r, z, t)$ of the azimuthal normal modes $-m_{\max} \leq m \leq m_{\max}$ is solved with the FTCS algorithm. Pressure and velocity fields are iteratively adjusted to each other with the method of ‘artificial compressibility’ (Peyret & Taylor 1985):

$$dp^{(n)} = -\beta \nabla \cdot \mathbf{u}^{(n)} \quad (0 < \beta < 1), \quad (2.3)$$

$$p^{(n+1)} = p^{(n)} + dp^{(n)}, \quad (2.4)$$

$$\mathbf{u}^{(n+1)} = \mathbf{u}^{(n)} - \Delta t \nabla (dp^{(n)}). \quad (2.5)$$

The pressure correction $dp^{(n)}$ in the n th iteration step, being proportional to the divergence of $\mathbf{u}^{(n)}$, is used to adapt the velocity field $\mathbf{u}^{(n+1)}$. The iteration loop (2.3)–(2.5) is executed for each azimuthal Fourier mode separately. It is iterated until $\nabla \cdot \mathbf{u}$ has become sufficiently small for each m mode considered – the magnitude of the total divergence never exceeded 0.02 and typically it was much smaller. After that the next FTCS time step is executed.

For code validation, we compared travelling and non-travelling solutions within a wide range of wavenumbers ($1.6 < k < 6$) with experiments (e.g. Heise *et al.* 2008a) and with previous numerical simulations (Büchel *et al.* 1996) and close to onset also

with Ginzburg–Landau results (Recktenwald, Lücke & Müller 1993). Furthermore, we compared bifurcation thresholds of nonlinear solutions with the respective stability boundaries of the linearized NSE (Langford *et al.* 1988) obtained by a shooting method that is described by Pinter, Lücke & Hoffmann (2003). As expected from our experience with primary vortex structures in the Taylor–Couette and Rayleigh–Bénard problem, the G1D3 FTCS bifurcation thresholds for our discretization typically lie 1%–2% below the respective linear stability thresholds. This deviation significantly reduces for finer discretization. We also investigated how the nonlinear solutions change when varying m_{max} and/or the grid spacing. From these analyses, we conservatively conclude that typical spiral frequencies have an error of less than about 0.2% and that typical velocity field amplitudes of non-propagating vortices can be off by significantly less than 3%–4%. Time steps were always well below the von Neumann stability criterion and by more than a factor of three below the Courant–Friedrichs–Lewy criterion. We found an error depending on the variation of time steps to lie below 1%. Neither higher radial and axial resolutions nor higher maximal azimuthal mode numbers lead to a significantly improved accuracy of the observed structures.

In order to approximate the case of infinitely long cylinders without axial lids, we performed a linear stability analysis of the basic flow for an axially periodic system ($\lambda = 2\pi/k$) using a shooting method. Any linear stability thresholds of axisymmetric $m = 0$ modes presented here are critical curves – they correspond to the onset of Taylor-vortex flow (TVF) in the axial infinite system.

2.2. Experimental setup

In the experiments the inner cylinder is machined from stainless steel having a radius of $r_1 = (12.50 \pm 0.01)$ mm, while the outer cylinder is made from optically polished glass with a radius of $r_2 = (25.00 \pm 0.01)$ mm. This results in a gap width $d = r_2 - r_1 = (12.50 \pm 0.02)$ mm and a radius ratio $\eta = r_1/r_2 = 0.5$ which is held fixed for all measurements. At top and bottom the fluid is confined by solid endwalls which are held fixed in the laboratory frame. The distance between these walls defines the axial height L of the flow which is adjustable within an accuracy of 0.01 mm.

The rotation of the cylinders is controlled by a PLL-unit achieving an accuracy of $\Delta f/f \propto 10^{-4}$ in the short-term and $\Delta f/f \propto 10^{-7}$ in the long-term average. As a working fluid within the gap between the two concentric cylinders a silicone oil with a density $\rho = 0.93$ g/cm³ and a kinematic viscosity $\nu = (10.6 \pm 0.1)$ cSt is used. The uncertainty of ± 0.1 cSt refers to the measurement of the absolute value of kinematic viscosity. The accuracy of ν during a measurement is primarily determined by the temperature variation of the fluid that is thermostatically controlled to (24.00 ± 0.01) °C. This yields $\Delta\nu = \partial\nu/\partial T|_{24.00\text{ °C}}\Delta T \approx 0.0025$ cSt. Though the uncertainty in the absolute value of ν introduces an uncertainty of the Reynolds numbers $\Delta R_{abs}/R \propto 10^{-2}$ in the absolute value of R the variation in Reynolds number with time is within $\Delta R/R \propto 10^{-4}$ during a measurement. This variation determines the resolution in Reynolds numbers that is achieved in the experiment.

For flow visualization purposes, 0.2% aluminium flakes with a length of 80 μm are added to the fluid. Flow visualization measurements are performed by monitoring the system with a CCD-camera in front of the cylinder recording the luminosity along a narrow axial stripe. The spatio-temporal behaviour of the flow is then represented by successive stripes for each time step at a constant φ position leading to continuous space–time plots.

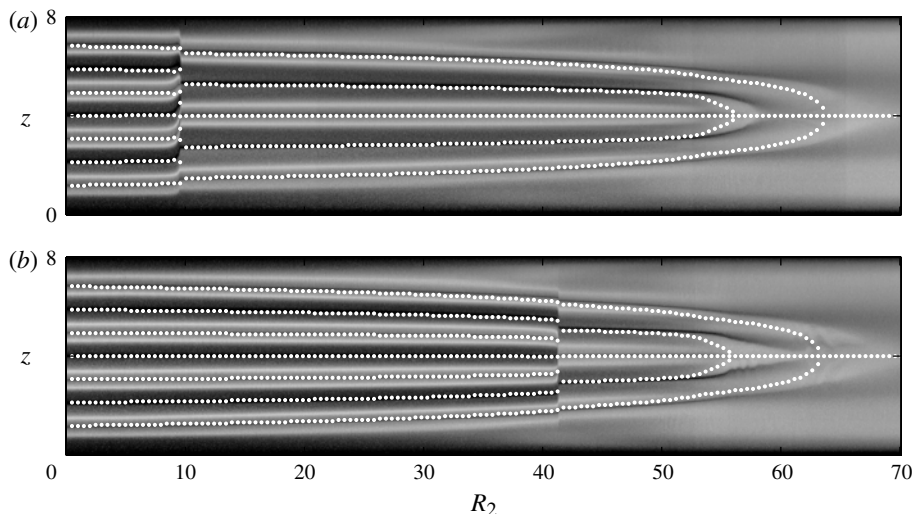


FIGURE 1. Space–time plots of experimentally obtained flow visualization (grey coded) and numerically (white dotted lines) obtained vortex boundaries of flow states for fixed inner cylinder rotation $R_1 = 130$ and system length $\Gamma = 8$ while quasi-statically decreasing (a) and increasing (b) outer cylinder rotation R_2 . Step sizes of both R_2 ramps are 0.5 in experiments as well as in simulations. Time steps are one diffusion time per R_2 step.

Especially for the determination of bifurcation points we utilize laser Doppler velocimetry (LDV). These measurements have always been performed at a fixed axial, radial and azimuthal position (r, φ, z) (see Heise *et al.* 2008a for details).

3. Results

3.1. Axisymmetric flow states

We start our discussion with the investigation of different axisymmetric states each consisting of an even number of vortices with the azimuthal wavenumber $m = 0$. All these states can be distinguished by the number of vortices, which strongly depends on the control parameters R_1 and R_2 and the system length Γ . Note that for inner-cylinder rotation rates $R_1 \gtrsim 180$ non-axisymmetric states are also observed.

For fixed $\Gamma = 8$ and $R_1 = 130$ (cf. red arrow in figure 3a), the number of vortices varies significantly with R_2 as shown in the space–time plots of figure 1. There, axial cuts of the flow are depicted for quasi-statically decreasing (a) and increasing (b) R_2 . The figure combines experimental (grey coded reflection intensity from flow visualization measurements given by the local orientation of the aluminium flakes) as well as numerical results (white dotted lines denoting the zeros of the axial velocity component w at mid-gap). The latter indicate the vortex boundaries and are an adequate measure to determine the axial wavenumber.

For stronger co-rotation ($R_2 \gtrsim 65$), a pair of two large vortices (2V state) exists driven by the non-rotating lids at the axial ends. This 2V state undergoes for decreasing R_2 (figure 1a) a sequence of transitions to states with four cells (4V)

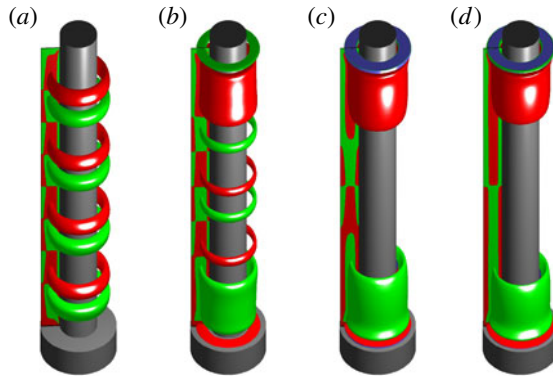


FIGURE 2. Four different flow visualizations for the axisymmetric flow states as illustrated in figure 1 at different R_2 . Therefore numerically determined iso-surface plots of the azimuthal vorticity $\Omega_\varphi = \partial_z u - \partial_r w$ are used in order to describe the topology of the vortices. Red refers to positive vorticity and green to negative vorticity. (a) 8V: $R_2 = 5$ ($\Omega_\varphi = \pm 75$), (b) 6V: $R_2 = 45$ ($\Omega_\varphi = \pm 70$), (c) 4V: $R_2 = 57$ ($\Omega_\varphi = \pm 40$) and (d) 2V: $R_2 = 70$ ($\Omega_\varphi = \pm 10$). Other control parameters for all simulations are $\Gamma = 8$ and $R_1 = 130$.

at $R_2 \approx 63$, six cells (6V) at $R_2 \approx 53$, and finally eight cells (8V) at $R_2 \approx 10$. These multi-cell states are characterized by equally distributed small vortices in the bulk with one significantly larger vortex near each axial end. In figure 1(b), the reverse transition sequence is observed for increasing R_2 starting with an 8V state at $R_2 = 0$. The latter exhibit a strong hysteresis and become unstable at $R_2 \approx 42$ against a 6V state. On the other hand, the transitions from 6V to 4V and from 4V to 2V are found to be non-hysteretic within the experimental and numerical accuracy. While a non-hysteretic transition is well-known for the onset of Taylor cells and therefore expected for the primary 2V–4V transition, the apparent absence of hysteresis in a secondary transition, i.e. between 4V and 6V, is unexpected. Note that the inertia of the aluminium particles used in the experimental setup together with small velocities lead to a blurred image, especially of the transitions to 4V and to 2V.

In order to give a three-dimensional impression of the flow states that are depicted in figure 1, the four axisymmetric flow states that appear are illustrated in figure 2 by the numerically determined iso-surface plots of the azimuthal vorticity $\Omega_\varphi = \partial_z u - \partial_r w$. Red refers to positive vorticity and green to negative vorticity (Altmeyer & Hoffmann 2010). The flow states are all observed at the same control parameters $\Gamma = 8$ and $R_1 = 130$, but different R_2 values – (a) 8V: $R_2 = 5$, (b) 6V: $R_2 = 45$, (c) 4V: $R_2 = 57$ and (d) 2V: $R_2 = 70$. Qualitatively the same scenario is observed for other values than $R_1 = 130$. The numerically determined phase diagram for $\Gamma = 8$ depicted in figure 3(a) therefore solely contains the non-hysteretic transitions between the different multi-cell states and gives a good impression of the stability of the multi-cell states. The long horizontal red arrow in this figure indicates the parameters used in figure 1. Additionally to figure 1, a two-cell state of different shape occurs for small R_1 and R_2 . This 2V' state is similar to the 2V state with the exception that each of the two vortices is bounded to its respective axial end and there exists a bulk with $w \equiv 0$ which furthermore increases its axial extent with decreasing R_2 . Note that the transition between 2V and 2V' is smooth.

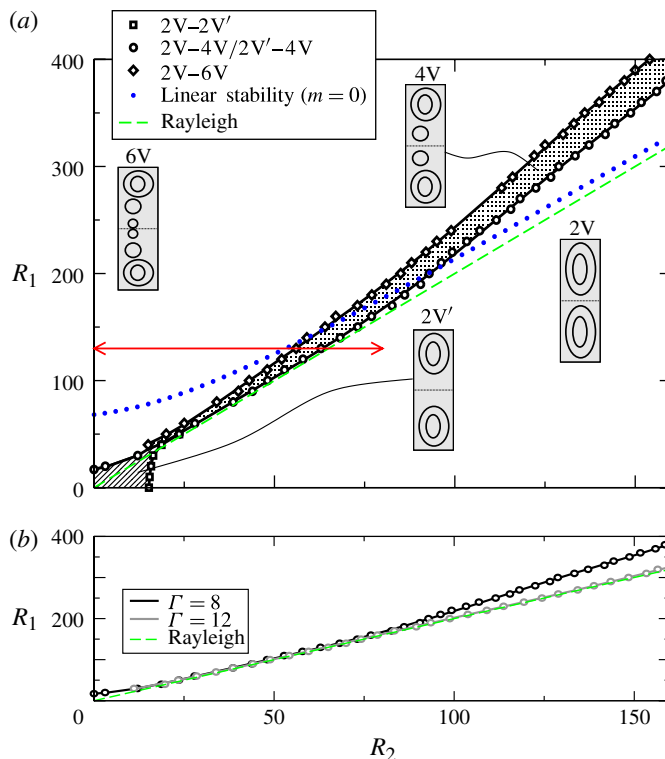


FIGURE 3. (a) Numerically determined phase diagram of multi-cell states for $\Gamma = 8$. All states are obtained by quasi-statically varying R_2 at different fixed R_1 . The numerical simulations were restricted to the $m = 0$ -Fourier subspace of only axisymmetric solutions of the Navier–Stokes equations. Different multi-cell states are labelled with sketches which roughly describe the vortex configuration in the (r, z) -plane of the annulus. To guide the eyes, the region of the $2V'$ state is hatched and that of the $4V$ state is coloured with grey. The blue dotted line of critical R_1 (resulting from linear stability analysis) describes the onset of TVF in the axially infinite system. The long horizontal red arrow indicates the parameters used in figure 1. (b) Comparison of the transition from the $2V$ state to the $4V$ state for $\Gamma = 8$ and $\Gamma = 12$. The Rayleigh curves are indicated as the dashed green line in both phase diagrams and it coincides very well with the $2V$ – $4V$ boundary for $\Gamma = 12$ in (b).

The blue dotted line in figure 3(a) denotes the critical linear stability threshold of TVF. For $R_2 \lesssim 90$, the TVF onsets lie above the multi-cell transition thresholds. Thus, as a consequence of the boundary-induced disturbances of the rigid lids, the multi-cell states occur below linear ($m = 0$) instability of CCF. In addition to that, the Rayleigh curves, given by $R_1 = 2R_2$ for our radius ratio are indicated as dashed green line in both phase diagrams in figure 3.

Figure 3(b) compares the $2V$ – $4V$ boundary for $\Gamma = 8$ with that for $\Gamma = 12$. For larger aspect ratios $\Gamma \gtrsim 12$, the respective $2V$ – $4V$ boundaries coincide very well with the Rayleigh criterion in the region being investigated (grey dashed line).

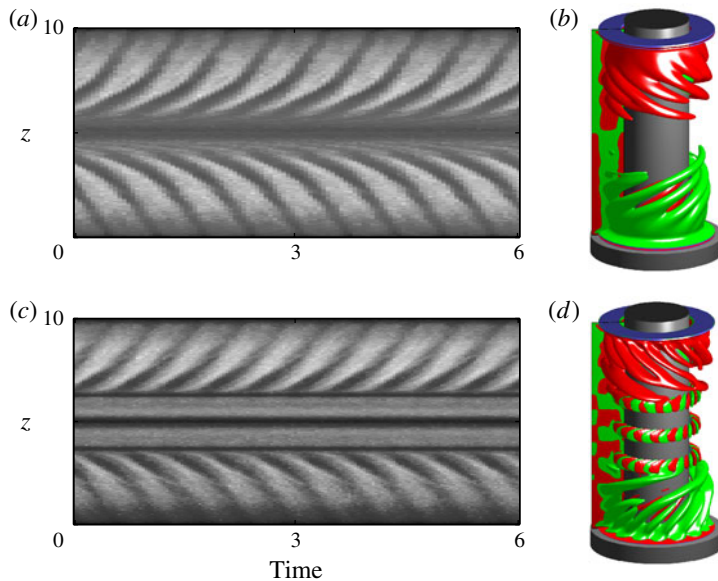


FIGURE 4. Flow visualizations of two different spiral states: one of them (*a,b*) contains two large Ekman vortices and the other (*c,d*) additionally contains a pair of small vortices at mid-height. (*a,c*) Experimentally obtained space–time plots. (*b,d*) Numerical simulations of the corresponding flow states with $\Omega_\varphi = \pm 95$ (*b*) and $\Omega_\varphi = \pm 90$ (*d*). Control parameters are $\Gamma = 10$ as well as (*a,b*) $R_1 = 318$, $R_2 = 160$ and (*c,d*) $R_1 = 247$, $R_2 = 110$.

3.2. Non-axisymmetric spirals

Owing to the restriction to $m = 0$ solutions, figure 3(*a*) contains no spirals. They occur in the unrestricted system for $R_1 \gtrsim 180$ close to the onset of the multi-cell states. These spiral states can be seen as a combination of upwards-propagating, left-winding spirals localized in the upper part and downwards-propagating, right-winding spirals localized in the lower part of the bulk. We verified that they bifurcate via a supercritical Hopf bifurcation either out of the 2V state or 4V state.

The phase-generating defect between the localized spiral states is similar to the P_+ defects in counter-rotating systems (Heise *et al.* 2008*b*). Depending on the control parameters, one finds two different types of such states as illustrated in the space–time plots in figure 4(*a,c*) and the iso-vorticity plots in figure 4(*b,d*) for two (R_1, R_2) parameter combinations marked by crosses in figure 5. The iso-surface plots of the vorticity $\Omega_\varphi = \pm 120$ describe the topology of the vortices. Red refers to positive vorticity, green to negative vorticity. Both states are very similar but differ significantly by the two small vortices which occur for the control parameters of figure 4(*c,d*) near the axial middle of the system. As a consequence of this superimposed two-cell mode, the radial flow at mid-height has switched from outflow in figure 4(*a,b*) to inflow in figure 4(*c,d*). However, the phase of both spirals is always generated near the adjacent outflow regions.

3.3. Stability

The phase diagram of figure 5(*a*) illustrates, for the same aspect ratio $\Gamma = 10$, the relation between the 2V–4V boundary and the onset of spirals. The shape

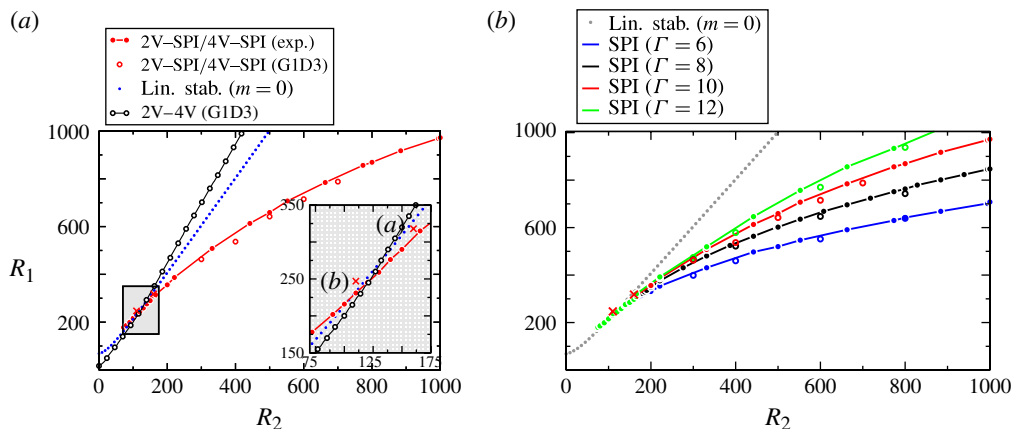


FIGURE 5. (a) Phase diagram of bifurcating spirals for a fixed aspect ratio $\Gamma = 10$. The solid red line with the filled circles indicates the experimentally obtained onset of the spirals and the corresponding open circles the numerically obtained onset. Additionally the numerically determined boundary between the 2V and the 4V multi-cell states is shown (black line with open circles) and the numerically calculated, dotted blue line denotes the critical linear stability threshold of axisymmetric ($m = 0$) solutions corresponding to the onset of TVF. The red crosses indicate the two control parameter values of both spirals depicted in figure 4. (b) Phase diagram of spiral flow for different aspect ratios (from bottom to top) $\Gamma = 6$ (blue), $\Gamma = 8$ (black), $\Gamma = 10$ (red), and $\Gamma = 12$ (green). The filled (open) circles indicate the experimentally (numerically) determined onsets of spirals for these aspect ratios. The grey dotted line denotes the numerically obtained critical linear stability threshold of axisymmetric ($m = 0$) solutions.

of the spiral structure of figure 4 is determined by the position of the respective control parameter combination relative to the 2V–4V boundary – figure 4(a,b) below, figure 4(c,d) above – as indicated by the crosses. The onset of these spirals (red) is determined experimentally by LDV measurements by quasi-statically increasing R_1 and analysing the corresponding time series for the frequency that appears. Additionally, the critical linear stability threshold for $m = 0$ (which corresponds to the onset of TVF in the axially infinite system) is plotted as the blue dotted line. This curve describes the lowest threshold where the basic CCF can become unstable in the axially infinite system – all the other critical stability curves for $m \neq 0$ lie above this curve (and are therefore not included here). Note that the spirals observed here do not appear in the infinite system. The endwall-induced axisymmetric vortex structure in the finite system, whose amplitude smoothly grows with increasing R_1 , is essential for these spirals to exist. The onset curves of these spirals and the multi-cell state cross the ($m = 0$) stability boundary of CCF in nearly the same control parameter regime. Thus, the spiral states corresponding to figure 4(a,b) bifurcate in the linear stable regime, those corresponding to figure 4(c,d) in the linear unstable regime. The spirals are triggered by the non-rotating lids and their onset therefore strongly depends on the aspect ratio Γ . The onsets of these spirals are illustrated in the experimentally observed (filled coloured circles) and numerically determined (open coloured circles) phase diagram of figure 5(b) for four different Γ . The bifurcation line of spiral vortices enters the Rayleigh stable regime at $R_1 \approx 130$. Therefore, time-dependent spirals dominate the

Rayleigh stable Taylor–Couette flow well below linear stability threshold even for a larger aspect ratio at sufficiently large R_2 .

4. Conclusions

Boundary-driven circulation plays a crucial role in the mode selection and the bifurcation behaviour in co-rotating Taylor–Couette flow and also in the Rayleigh stable regime. For stronger co-rotation, we found a dominant axisymmetric flow state consisting of two large vortices. On reducing the outer-cylinder Reynolds number R_2 , this state undergoes a sequence of partially hysteretic transitions to different axisymmetric multi-cell states. These transitions are always accompanied by a decrease of the wavelength of all bulk vortices and especially of the Ekman vortices.

Furthermore, we found spiral states in the Rayleigh stable regime bifurcating via a supercritical Hopf bifurcation out of the respective axisymmetric flow state (two cells or four cells). The shapes of these spiral states are strongly determined by the underlying axisymmetric multi-cell (n V) state, i.e. $m \neq 0$ disturbances may grow, even below the linear ($m = 0$) instability of CCF due to boundary-induced $m = 0$ modes which continuously stimulate $m \neq 0$ modes emerging out of $m \neq 0$ fluctuations.

While in the classical case of a non-rotating outer cylinder, the number of Taylor cells at onset corresponds basically to the value of the aspect ratio Γ (at least for Γ being an even multiple of the gap width), we found that in the co-rotating case the number of cells is four at onset, i.e. two large Ekman cells and two small Taylor cells in the bulk of the system. This is an interesting new finding with possible implications for the multiplicity of states and mode interaction in the co-rotating regime.

Stability and turbulent transport of angular momentum in co-rotating Taylor–Couette flow have also attracted considerable attention in recent years with respect to the understanding of astrophysical disks. (cf. Hollerbach & Rüdiger 2005; Duschl & Britsch 2006; Ji *et al.* 2006; Stefani *et al.* 2006; van Gils *et al.* 2011; Paoletti & Lathrop 2011; Avila 2012).

Though secondary circulation induced by endwalls in experimental setups is often reduced by suitable endwall rotation (Abshagen *et al.* 2004; Hollerbach & Fournier 2004; Burin *et al.* 2006; Schartman *et al.* 2009; Altmeyer *et al.* 2010), global endwall effects can alter the stability behaviour of co-rotating Taylor–Couette flow (Avila *et al.* 2008). Our combined experimental and numerical work allows insights into the solution structure of Rayleigh-stable flows having strong axial variation of angular momentum.

Acknowledgements

We acknowledge support from the Deutsche Forschungsgemeinschaft.

References

- ABSHAGEN, J., HEISE, M., PFISTER, G. & MULLIN, T. 2010 Multiple localized states in centrifugally stable rotating flow. *Phys. Fluids* **22**, 1–4.
- ABSHAGEN, J., LANGENBERG, J., PFISTER, G., MULLIN, T., TAVENER, S. J. & CLIFFE, K. A. 2004 Taylor–Couette flow with independently rotating end plates. *J. Theor. Comput. Fluid Dyn.* **18**, 129–136.
- ALTMAYER, S. & HOFFMANN, CH. 2010 Secondary bifurcation of mixed-cross-spirals connecting travelling wave solutions. *New J. Phys.* **12** (11), 113035.

Co-rotating Taylor–Couette flow enclosed by stationary disks

- ALTMAYER, S., HOFFMANN, CH., HEISE, M., ABSHAGEN, J., PINTER, A., LÜCKE, M. & PFISTER, G. 2010 End wall effects on the transitions between Taylor vortices and spiral vortices. *Phys. Rev. E* **81** (6), 066313.
- ANDERECK, C. D., LIU, S. S. & SWINNEY, H. L. 1986 Flow regimes in a circular Couette system with independently rotating cylinders. *J. Fluid Mech.* **164**, 155–183.
- AVILA, M. 2012 Stability and angular-momentum transport of fluid flows between corotating cylinders. *Phys. Rev. Lett.* **108**, 124501.
- AVILA, M., GRIMES, M., LOPEZ, J. M. & MARQUES, F. 2008 Global endwall effects on centrifugally stable flows. *Phys. Fluids* **20**, 104104.
- BENJAMIN, T. B. 1978 Bifurcation phenomena in steady flows of a viscous fluid. I. Theory. *Proc. R. Soc. Lond. A* **359**, 1–26.
- BENJAMIN, T. B. 1978 Bifurcation phenomena in steady flows of a viscous fluid. II. Experiments. *Proc. R. Soc. Lond. A* **359**, 27–43.
- BENJAMIN, T. B. & MULLIN, T. 1981 Anomalous modes in the Taylor experiment. *Proc. R. Soc. Lond. A* **377**, 221–249.
- BÜCHEL, P., LÜCKE, M., ROTH, D. & SCHMITZ, R. 1996 Pattern selection in the absolutely unstable regime as a nonlinear eigenvalue problem: Taylor vortices in axial flow. *Phys. Rev. E* **53**, 4764–4777.
- BURIN, M., JI, H., SCHARTMAN, E., CUTLER, R., HEITZENROEDER, P., LIU, W., MORRIS, L. & RAFTOPOLOUS, S. 2006 Reduction of Ekman circulation within Taylor–Couette flow. *Exp. Fluids* **40** (6), 962–966.
- CLIFFE, K. A., KOBINE, J. J. & MULLIN, T. 1992 The role of anomalous modes in Taylor–Couette flow. *Proc. R. Soc. Lond. A* **439** (1906), 341–357.
- CROSS, M. C. & HOHENBERG, P. C. 1993 Pattern formation outside of equilibrium. *Rev. Mod. Phys.* **65** (3), 851.
- CZARNY, O., SERRE, E., BONTOUX, P. & LUEPTOW, R. M. 2003 Interaction between Ekman pumping and the centrifugal instability in Taylor–Couette flow. *Phys. Fluids* **15**, 467.
- DUSCHL, W. J. & BRITSCH, M. 2006 A gravitational instability-driven viscosity in self-gravitating accretion disks. *Astrophys. J. Lett.* **653** (2), 89–92.
- VAN GILS, D. P. M., HUISMAN, S. G., BRUGGERT, G.-W., SUN, CH. & LOHSE, D. 2011 Torque scaling in turbulent Taylor–Couette flow with co- and counterrotating cylinders. *Phys. Rev. Lett.* **106**, 024502.
- HEGSETH, J. J., BAXTER, G. W. & ANDERECK, C. D. 1996 Bifurcation from Taylor vortices between corotating concentric cylinders. *Phys. Rev. E* **53**, 507–521.
- HEISE, M., ABSHAGEN, J., HOCHSTRATE, K., KÜTER, D., PFISTER, G. & HOFFMANN, CH. 2008a Localized spirals in Taylor–Couette flow. *Phys. Rev. E* **77**, 026202.
- HEISE, M., HOCHSTRATE, K., ABSHAGEN, J. & PFISTER, G. 2009 Spirals vortices in Taylor–Couette flow with rotating endwalls. *Phys. Rev. E* **80** (4), 045301.
- HEISE, M., HOFFMANN, CH., ABSHAGEN, J., PINTER, A., PFISTER, G. & LÜCKE, M. 2008b Stabilization of domain walls between traveling waves by nonlinear mode coupling in Taylor–Couette flow. *Phys. Rev. Lett.* **100** (6), 064501.
- HIRT, C. W., NICHOLS, B. D. & ROMERO, N. C. 1975 SOLA: a numerical solution algorithm for transient fluid flows. *NASA STI/Recon Tech. Rep. N* **75**, 32418.
- HOLLERBACH, R. & FOURNIER, A. 2004 End-effects in rapidly rotating cylindrical Taylor–Couette flow. In *MHD Couette Flows: Experiments and Models*, vol. 733, pp. 114–121.
- HOLLERBACH, R. & RÜDIGER, G. 2005 New type of magnetorotational instability in cylindrical Taylor–Couette flow. *Phys. Rev. Lett.* **95** (12), 124501.
- JI, H., BURIN, M., SCHARTMAN, E. & GOODMAN, J. 2006 Hydrodynamic turbulence cannot transport angular momentum effectively in astrophysical disks. *Nature* **444** (7117), 343–346.
- LANGFORD, W. F., TAGG, R., KOSTELICH, E. J., SWINNEY, H. L. & GOLUBITSKY, M. 1988 Primary instabilities and bicriticality in flow between counter rotating cylinders. *Phys. Fluids* **31**, 776–785.
- MULLIN, T. 1982 Mutations of steady cellular flows in the Taylor experiment. *J. Fluid Mech.* **121**, 207–218.
- NAGATA, M. 1988 On wavy instabilities of the Taylor-vortex flow between corotating cylinders. *J. Fluid Mech.* **88**, 585.

- PAOLETTI, M. S. & LATHROP, D. P. 2011 Angular momentum transport in turbulent flow between independently rotating cylinders. *Phys. Rev. Lett.* **106**, 024501.
- PEYRET, R. & TAYLOR, T. D. 1985 *Computational Methods for Fluid Flow*. Springer.
- PINTER, A., LÜCKE, M. & HOFFMANN, CH. 2003 Spiral and Taylor vortex fronts and pulses in axial through flow. *Phys. Rev. E* **67**, 026318.
- RECKTENWALD, A., LÜCKE, M. & MÜLLER, H. W. 1993 Taylor vortex formation in axial through-flow: linear and weakly nonlinear analysis. *Phys. Rev. E* **48**, 4444–4454.
- SCHARTMAN, E., JI, H. & BURIN, M. 2009 Development of a Couette–Taylor flow device with active minimization of secondary circulation. *Rev. Sci. Instrum.* **80**, 024501.
- STEFANI, F., GUNDRUM, T., GERBETH, G., RÜDIGER, G., SCHULTZ, M., SZKLARSKI, J. & HOLLERBACH, R. 2006 Experimental evidence for magnetorotational instability in a Taylor–Couette flow under the influence of a helical magnetic field. *Phys. Rev. Lett.* **97** (18), 184502.
- TAGG, R. 1994 The Couette–Taylor problem. *Nonlinear Sci. Today* **4** (3), 1–25.
- TAVENER, S. J. & CLIFFE, K. A. 1991 Primary flow exchange mechanisms in the Taylor apparatus applying impermeable stress-free boundary conditions. *IMA J Appl. Maths* **46**, 165–199.
- TAYLOR, G. I. 1923 Stability of a viscous liquid contained between two rotating cylinders. *Phil. Trans. R. Soc. Lond. A* **223**, 289–343.